A Nanocavitation Approach to Understanding Water Capture, Water Release, and Framework Physical Stability in Hierarchically Porous MOFs

Jian Liu,[†,‡,*] Jesse L. Prelesnik,[§] Roshan Patel,[§,‖] Boris V. Kramar,[†] Rui Wang,[†] Christos D. Malliakas,[†] Lin X. Chen,[†,⊥] J. Ilja Siepmann,[§,‖,*] and Joseph T. Hupp[†,*]

[†] Department of Chemistry, Northwestern University, 2145 Sheridan Road, Evanston, IL 60208, United States.

[‡] School of Chemistry and Materials Science, Rochester Institute of Technology, Rochester, NY, 14623, United States.

[§] Department of Chemistry and Chemical Theory Center, University of Minnesota, 207 Pleasant Street SE, Minneapolis, MN 55455, United States.

[‖] Department of Chemical Engineering and Materials Science, University of Minnesota, 412 Washington Avenue SE, Minneapolis, MN 55455, United States.

[⊥] Chemical Sciences and Engineering Division, Argonne National Laboratory, Argonne, Illinois 60439, United States.

KEYWORDS: Hierarchically Porous MOFs, Nanocavitation, Framework Stability, Water Capture & Release, Difference Envelope Density (DED), Molecular Dynamics Simulations.

ABSTRACT: Chemically-stable metal–organic frameworks (MOFs) featuring interconnected hierarchical pores have proven promising for a remarkable variety of applications. Nevertheless, framework susceptibility to capillary-force-induced pore collapse, especially during water evacuation, has often limited practical applications. Methodologies capable of predicting the relative magnitudes of these forces as functions of pore size, chemical composition of the pore walls, and fluid loading would be valuable for resolution of the pore collapse problem. Here, we report that a molecular simulation approach centering on evacuation-induced nanocavitation within fluids occupying MOF pores can yield the desired physical-force information. The computations can spatially pinpoint evacuation elements responsible for collapse and the chemical basis for mitigation of collapse of modified pores. Experimental isotherms and difference-electron-density measurements of the MOF NU-1000 and four chemical variants validate the computational approach and corroborate predictions regarding relative stability, anomalous sequence of pore-filling, and chemical basis for mitigation of destructive forces.

INTRODUCTION

The broad synthetic availability of metal–organic frameworks (MOFs) that are chemically stable toward water has opened-up applications in vapor- and condensed-phase chemical separations, bio-catalysis, chemical catalysis capture of aqueous pollutants, and even water-harvesting from low-humidity environments.[1-5] Essential for these applications is chemical stability of the framework itself toward hydrolysis, where the point of hydrolytic attack typically is the MOF node:linker junction. The factors responsible for such stability are reasonably well understood; they include: a) framework hydrophobicity, b) thermodynamically strong node-linker bonding, and/or c) kinetically-inert/substitution-resistant node-linker bonding.[6-9]

When polar functional groups imbue pore walls with hydrophilic character, MOF pores can spontaneously fill with water when exposed to humid atmospheres, where the required relative humidity (RH) can be as low as 10%.[10] Indeed, spontaneous pore-filling is key to certain applications – most notably, cyclical water-harvesting,[11] heat-pump behavior,[12] and hydrolytic degradation of volatile chemical threats.[13-14] Subsequent decrease of the RH leads to evaporative removal of pore-condensed water. Accompanying the removal are attractive (*i.e.*, inward directed) capillary forces that can collectively engender mechanical fracture of node–linker bonds, collapse of MOF channels/pores, and degradation of MOF performance.[14] Qualitatively, collapse due to capillary forces tends to be more prominent for hydrophilic than hydrophobic pores and for mesopores compared to micropores. Nevertheless, for mesoporous (> 2 nm), microporous (< 2 nm), and hierarchically porous MOFs, performance-predictive elucidation and quantification of these forces has proven elusive. Indeed, in a recent perspective/review article on water harvesting, Hanikel and co-authors remarked,[11] regarding MOF stability, that: "hydrolysis can easily be predicted based on basic chemical principles and steric effects, but architectural stability is rather difficult to predict...". For MOF "architectural stability", the predictive computational challenges stem, in part, from the molecular granularity of real solvents. Granularity renders the continuum-fluid-based Kelvin equation inadequate on the length scales typical of MOF pores. The challenges also stem from strong hydrogen-bonding interactions between captured solvent molecules and between these molecules and the host framework.

Here, we describe a molecular-simulation-based nanocavitation approach to quantifying potentially MOF-destructive capillary forces. This approach derives from our previous work on density-depletion-induced formation of

https://doi.org/10.26434/chemrxiv-2023-rvvfr **ORCID:** https://orcid.org/0000-0002-5024-1879 Content not peer-reviewed by ChemRxiv. **License:** CC BY-NC-ND 4.0

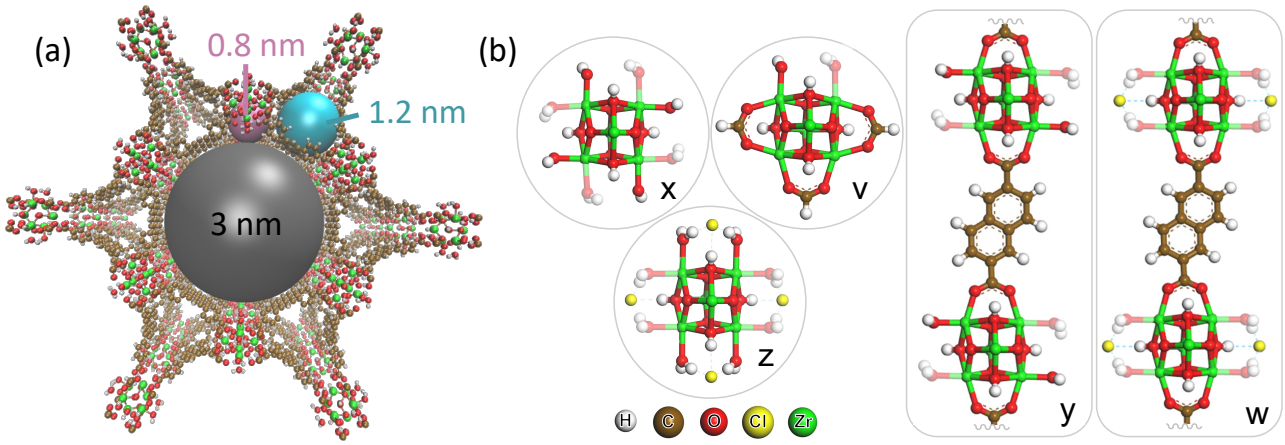

Figure 1. (a) Structural representation of NU-1000, a Zr-MOF, featuring a **csq** topology, that consists of $Zr_6(\mu_3\text{-}O)_4(\mu_3\text{-}OH)_4(H_2O)_4(OH)_4^{8+}$ (Zr_6) nodes and tetratopic 1,3,6,8-tetrakis(p-benzoate)pyrene ($TBAPy^{4-}$) linkers. The characteristic 1D hexagonal and triangular channels (*ca.* 3.0 and 1.2 nm in diameter, respectively) along the crystallographic *c* axis are cross-connected by pores of ca. 0.8 nm diameter; (b) Node structures of NU-1000 variants, including (x) NU-1000, (v) NU-1000-Formate, (z) NU-1000-Cl, (y) NDC-NU-1000, and (w) NDC-NU-1000-Cl. Aqua and hydroxyl ligands on the variable nodes provide hydrogen bond donor and acceptor sites for interactions with water molecules. Transparent aqua ligands were removed after vacuum-heated dehydration treatment.

nanobubbles in water.[15] We apply it to water uptake and release from several versions of NU-1000,[16-20] a MOF that is chemically stable in water, but susceptible to physical collapse during water evacuation.[21-22] NU-1000 is characterized by 1D hexagonal and triangular channels of *ca.* 3.0 and 1.2 nm diameter, respectively, aligned along the crystallographic *c* axis. The channels are cross-connected by pores of *ca.* 0.8 nm diameter (**Figure 1a**). We find that the overall computational approach reproduces experimental water-sorption isotherms, accounts for isotherm differences for variants of NU-1000 and unveils the sequence of pore-filling for these architecturally complex materials – a sequence that is, for the first time, experimentally validated by difference electron density (DED) analysis of powder X-ray diffraction (PXRD) data collected at differing RHs. The nanocavitation component of the computations yields mechanically relevant values for the otherwise elusive capillary force(s) across the entire range of vapor-pressure driven pore evacuation. The nanocavitation treatment also pinpoints the evacuation steps responsible for pore collapse and reveals why seemingly minor chemical modifications to the MOF impart salutary resistance to framework collapse. Finally, by introducing statistical-mechanics concepts, such as the virial pressure, the nanocavitation treatment yields useful, MOF-generalizable, mechanical and structural insight into stabilization of these ubiquitous materials against sorbate-caused framework collapse.

RESULTS AND DISCUSSION

We hypothesize that in addition to contributions from weak dispersion interactions, substantial pore-destabilizing capillary-force contributions might derive from comparatively strong and directional hydrogen-bonding interactions between channel-sited water molecules and the O-H rich nodes of NU-1000 (sixteen O-H bonds/node in **Figure 1b-x**, deriving from bridging-hydroxo, terminal-hydroxo, and terminal aqua ligands). We further hypothesize that H-bonding contributions could be systematically diminished by introducing NDC^{2-} (naphthalene-dicarboxylate) as an auxiliary structural ligand along the MOF *c*-axis to make NDC-NU-1000 (**Figure 1b-y**) or by converting terminal aqua/hydroxo ligand pairs to aqua/aqua pairs and then hydrogen-bonding these ligands to charge-balancing second-sphere chloride ions to make NU-1000-Cl (**Figure 1b-z**). Each incorporated NDC eliminates two aqua/hydroxo ligand pairs.[19] From single-crystal X-ray diffraction measurements, each second-sphere chloride hydrogen-bonds with two node aqua ligands.[16]

We note that as-synthesized NU-1000, if conventionally activated *via* heating in dimethylformide + aq. HCl, recruits ~ 3 node-bridging formate ions/Zr_6;[20,23] these displace three aqua/hydroxo ligand pairs to yield NU-1000-Formate (**Figure 1b-v**). While indefinitely persistent in vacuum, we have previously shown that MOF immersion in liquid water leads, within hours, to loss of adventitious formate ions and replacement by aqua/hydroxo ligand pairs. Thus, on the timescales relevant for experimental measurements (water isotherms, DEDs, and solid-state NMR), formate is anticipated to: a) desorb if sufficient water is present, and therefore, b) exert little influence upon NU-1000 stability against water-engendered pore collapse. Nevertheless, for completeness, we also included results for NU-1000-Formate. To understand how a formate-like entity would affect stability if desorption could be suppressed, we have intentionally neglected formate labilization in computations.

Synthesis and Characterization. NU-1000, NU-1000-Cl, NU-1000-Formate, NDC-NU-1000, and NDC-NU-1000-Cl were synthesized using previously reported procedures and detailed characterization can be found in these reports.[16-19] Benzoic acid and trifluoroacetic acid were used as modulators to suppress unwanted co-crystallization and mixed crystallization of NU-901, a polymorph of NU-1000.[24-25] With the combined aims of: a) removing modulators, b) avoiding replacement of coordinated modulators with coordinated solvent-decomposition products, *e.g.* formate, c) avoiding synthesis-solvent coordination, and d) adding Cl^- to the second coordination-sphere of NU-1000's Zr_6-oxy

https://doi.org/10.26434/chemrxiv-2023-rvvfr **ORCID:** https://orcid.org/0000-0002-5024-1879 Content not peer-reviewed by ChemRxiv. **License:** CC BY-NC-ND 4.0

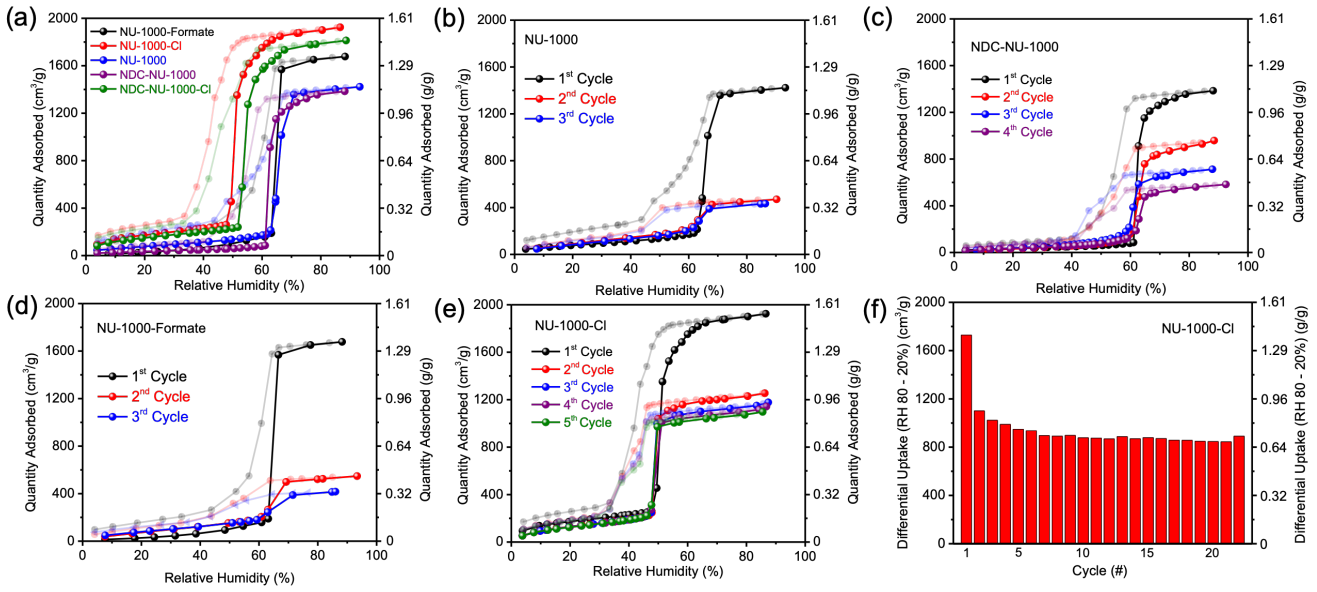

Figure 2. (a) First-cycle plots of gravimetric uptake (bold) and release (light) of water vapor (298 K) by five variants of thermally-treated NU-1000 showing cm^3 and gram of water adsorbed per gram of MOFs vs. RH, (b) Three to five successive water-vapor adsorption/desorption isotherms for NU-1000, (c) NDC-NU-1000, (d) NU-1000-Formate, and (e) NU-1000-Cl. (f) Differential gravimetric water uptake between RH=80% and 20% with NU-1000-Cl for twenty-two cycles.

node, and charge-balancing H^+ to the node's first coordination-sphere *via* terminal hydroxo-to-aqua ligand conversion, as-synthesized MOFs were treated with HCl in dioxane at ambient temperature.[16,18] Repetitive rinsing with weakly basic aqueous triethylamine accomplishes aqua-to-hydroxo ligand conversion, removes chloride, and yields node-accessible NU-1000 – elsewhere termed NU-1000-FF for formate-free.[16-18] X-ray absorption spectroscopy (**Figures S1-S8 & Tables S1-S8**) further informed us regarding node coordination, while X-ray photoelectron spectroscopy was used to determine the Cl loading (**Figure S9**).

Water Adsorption-Desorption Isotherms. Samples were vacuum-heated (120°C) to remove physisorbed solvent. Also removed are node aqua ligands,[17-18] where the number removed ranges from ~1 to 8; see **Figure 1b**. In contrast, NDC and formate are retained, as is second-sphere chloride – albeit, *via* reversible coordination by Zr(IV) (**Tables S1, S5 & S8**). From **Figure 2a**, and consistent with the presentation of three pore-types, water pore-filling for all five variants occurs in three stages: gradual filling to no more than 10% of saturation; starting at ~50-60% RH, rapid filling to *ca.* 90% of saturation; further gradual filling toward saturation. For guest-host systems with stronger guest-host interactions than guest-guest interactions (usually the case for argon and N_2), pores are filled in order from smallest to largest. Here the order is strikingly different, with NU-1000's largest pores – high-volume mesoporous channels – being filled mainly in the second stage of water uptake, likely reflecting an outsized role for guest-host and guest-guest H-bonding.

From **Figure 2a**, incorporation of second-sphere chloride (NU-1000-Cl and NDC-NU-1000-Cl) shifts the onset of the steep uptake from ~ 60% to ~ 50% RH, no doubt reflecting enhanced mesopore hydrophilicity.[26-29] **Table S9** summarizes 1st-cycle gravimetric uptake data at RH = 90% and 298 K for all versions NU-1000 examined. **Figures S10-S15** reveals a rough proportionality between water uptake and total pore volume as determined from N_2 isotherms. For some applications, a more meaningful metric is volumetric uptake (cm^3 water/cm^3 sorbent). **Table S10** shows that the Cl-containing MOFs reach ~ 940 cm^3/cm^3, placing them the highest among the materials in our study.

At RH <50%, water uptake is defined mainly by *c*-pore filling – both conventional sorption and re-recruitment of node aqua ligands. The differences in uptake in **Figure 2a** are attributable, in part, to differences in the number of aqua ligands recruited. Note that in the absence of heating, aqua ligands are retained in subsequent desorption cycles. For all samples, mesopore evacuation is characterized by hysteresis – an expected finding when pore diameters exceed ~22 Å, and a signature of fluid cavitation during evacuation.[11]

Figures 2b reveals a catastrophic loss of uptake capacity for NU-1000 in the 2nd cycle, attributable to capillary-force induced mesopore collapse in the 1st desorption half-cycle.[22] **Figure 2c** shows that buttressing the MOF with secondary structural ligands along the *c*-axis is ineffective in suppressing collapse. The relevant components of the channel-collapsing force evidently are cross-sectionally directed. **Figure 2d** shows that replacing hydrophilic aqua/hydroxo pairs with formate ligands (with the non-polar C-H group pointing toward the pore interior) does not stop capacity loss – consistent with the known susceptibility of formate toward gradual displacement when pores are water-infiltrated.[22,30] In contrast, introduction of chlorides as second-sphere ligands engenders a remarkable and salutary partial-suppression of subsequent capacity loss[29] that persists for at least twenty cycles (**Figures 2e, 2f, and S15**).

Guided by the insights from molecular simulations, we also restricted humidity cycling to low, intermediate, or high ranges (**Figures 3a,b**) to pinpoint the part of the desorption process that leads to structural damage.

https://doi.org/10.26434/chemrxiv-2023-rvvfr **ORCID:** https://orcid.org/0000-0002-5024-1879 Content not peer-reviewed by ChemRxiv. **License:** CC BY-NC-ND 4.0

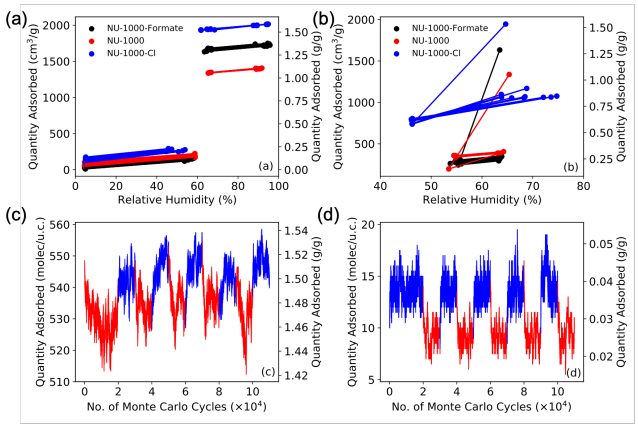

Figure 3. (a) Ten successive water adsorption-desorption cycles, stepping between RH=5 and 55%, then between 65 and 90% for NU-1000 and NU-1000-Formate, and between 5 and 45%, followed by 65-90%, for NU-1000-Cl. (b) Ten successive water adsorption-desorption cycles for NU-1000 & NU-1000-Formate between RH ~55 and ~65%, and for NU-1000-Cl between RH ~45 and ~65%. Adsorption-desorption cycling of water in NU-1000 at high (c) and low (d) RH conditions from NpT-GEMC simulations. The progression of the water loading during adsorption and desorption segments are shown in blue and red, respectively. Beyond the initial period, each segment consists of 10,000 MC cycles. The cycling at high RH is from 70% to 100%, and for low RH is from 5% to 65%.

No capacity loss is engendered by repetitively partially evacuating frameworks at low or high RHs, and it is apparent that MOF collapse derives exclusively from evacuation of mesopores at intermediate RH.

DED Assessment of Water Siting. PXRD data (**Figures S16-S21**) collected in the presence and absence of humidity can be used to locate adsorbed water – evident as excess electron density – within the corresponding hierarchically porous networks. These experiments (see **SI**) were executed in much the same fashion as previous reports of DED mapping of molecule, cluster, and nanoparticle siting within MOFs,[31-33] but with X-rays from a conventional source[34] rather than a high-intensity synchrotron. At low water loadings (20% and 50% RH (points (i) and (ii) in **Figure 4a,b**)), the observed water electron density is exclusively located in the ultramicroporous *c*-pore. As RH is increased to yield roughly half of the saturation loading (65% RH shown as (iii) in **Figure 4a,b**), water density spreads to the mesopores. Near saturation (90% RH shown as (iv) in **Figure 4a,b**), water density finally appears in triangular micropores. The nonstructural formate ligands do not change this sequential water capture process (**Figures S22-S26**). For NU-1000-Cl, which features eight aqua ligands and is already half-filled at 50% RH (**Figure 4d**), the detailed, pore-specific pattern of water uptake revealed by DED plots (**Figure 4c** (ii-iv)) is altered such that the mesopores fill more readily.

Generalizing, water begins to adsorb in the hydroxylated *c*-pore pocket between pairs of Zr_6 nodes, accumulates around the nodes and linkers in the mesopores to form larger water clusters at higher water loading, and eventually fills the most hydrophobic triangular micropores under conditions approaching saturation. This picture is supported by our computational studies discussed in detail below.

Solid-state ^{1}H Magic Angle Spinning (MAS) NMR. SSMAS ^{1}H NMR is increasingly used to explore chemical structures, dynamic behavior, and host-guest interactions in MOFs.[35-38] Results for exposure of thermally treated (*i.e.*, 0% RH) NU-1000, NU-1000-formate, and NU-1000-Cl to controlled-humidity atmosphere (*i.e.*, 50% RH) are presented and discussed in **Figure S27**. Resonances from higher water loading tends to overlap with other resonances and, hence, are excluded from this study. Briefly, the experiments reveal: a) repopulation of Zr_6 nodes with aqua ligands; b) hydrogen bond formation between node hydroxo ligands and incorporated water molecules; c) at high RH, formation of bulk-like water in the pores; but d) no perturbation of linker resonances by sorbed water molecules.

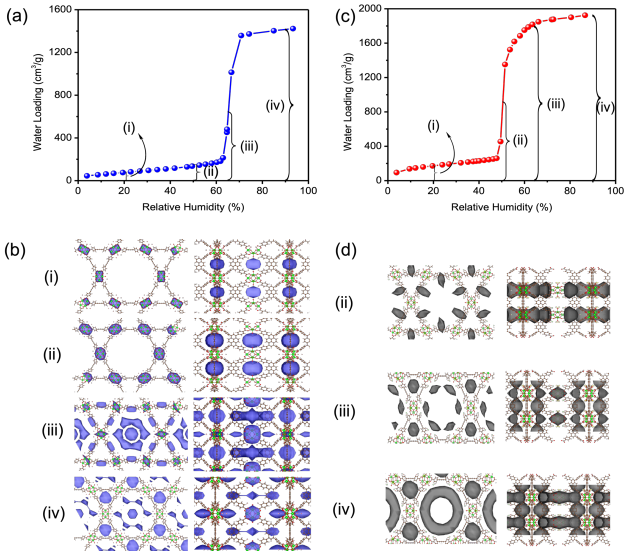

Figure 4. (a) Initial adsorption isotherm for NU-1000, with (b) DED maps of water siting at RHs of 20% (i), 50% (ii), 65% (iii), and 90%(iv). (c) and (d) present analogous plots for NU-1000-Cl. The electron density from 20% RH NU-1000-Cl ((i) in **(c)**) was used as background to obtain water sitting in NU-1000-Cl under higher RHs to avoid the influence from phase change in 0% RH NU-1000-Cl. Note, the left columns in **(b)** and **(d)** stand for the *a,b* plane of the hexagonal lattice, and the right columns stand for the perpendicular plane to *a,b* plane.

Molecular Simulations. These studies were aimed at understanding: a) *via* NpT Gibbs ensemble Monte Carlo (GEMC) simulations, the pore-sequence of water uptake and release, and b) *via* NVT molecular dynamics (MD) simulations (see **SI** for details), the water-loading-dependent magnitude of forces that may engender pore collapse – in each case, as a function of MOF-variant composition. Our approach to the latter relies upon recent (non-MOF) work on cavitation and nanobubble formation in water.[15] Briefly, the approach centers on computation of the virial pressure (P_{wat}) from intermolecular forces within the pores. Remarkably, when pore-confined water is present at densities (ρ_{wat}) less than that of unperturbed bulk water, P_{wat} can be negative. If stretched water (ρ_{wat}< bulk) undergoes a transition to bulk-like water + vapor nanobubbles, *i.e.* nanocavitation, the pressure effects due to the water molecules can be calculated. The virial pressure in this circumstance again can

https://doi.org/10.26434/chemrxiv-2023-rvvfr **ORCID:** https://orcid.org/0000-0002-5024-1879 Content not peer-reviewed by ChemRxiv. **License:** CC BY-NC-ND 4.0

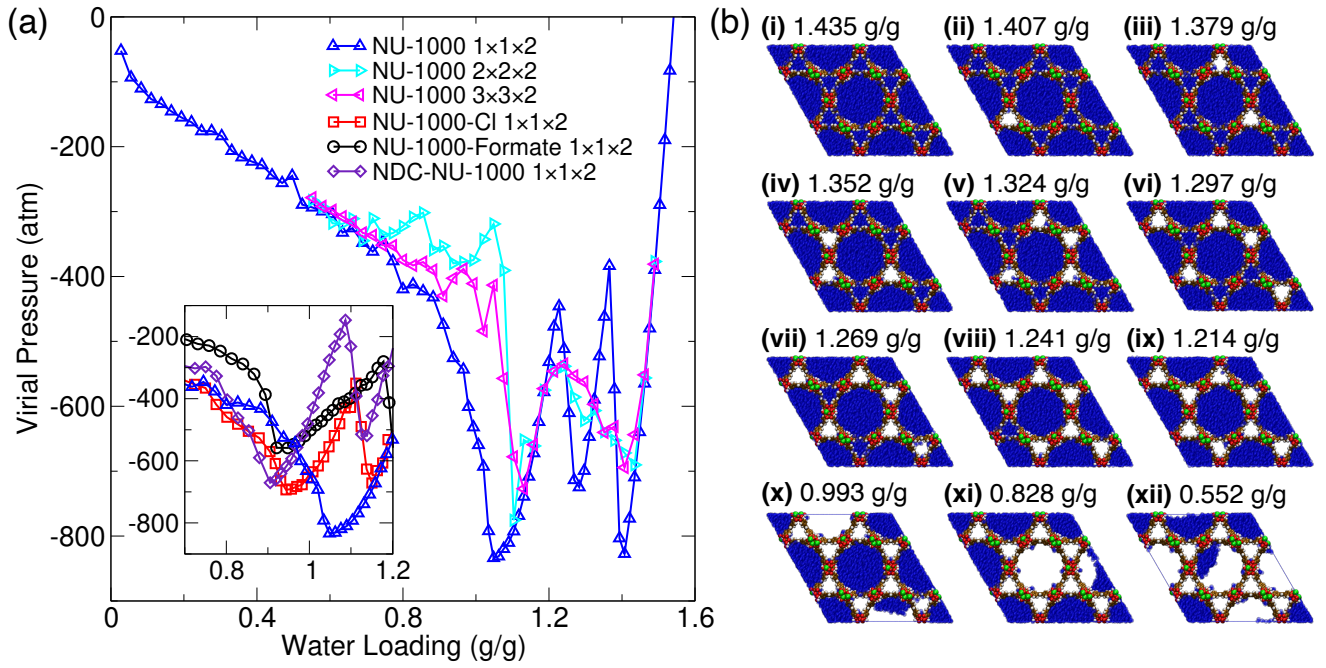

Figure 5. (a) Molecular simulation data for the virial pressure, the magnitude of which is a proxy for the contractive forces experienced by the framework, as a function of water loading for different chemical functionalization of the nodes. Lines connecting data points are a guide for the eye. The minimum near 1.0 g/g is pronounced in all system sizes investigated, while additional features seen above 1.2 g/g are washed out when larger systems are considered (**Figure S28**). The minimum near 1.0 g/g is deepest for NU-1000, while the addition of chloride partially mitigates this effect. Numerical data are provided in **Tables S11-S18**. (b) Representative simulation snapshots illustrating water localization tendencies as the framework is emptied for NU-1000 at a system size of 2×2×2 unit cells. From (i)-(ix), micropores evacuate sequentially. From (x)-(xii), mesopores evacuate sequentially. Note, water molecules are colored blue. The conversion factor from (g water)/(g MOF) to (cm^3 water vapor)/(g MOF) is 1244 cm^3/g.

be negative and can be viewed as a proxy for the collapse-inducing force experienced by MOF pores. The dependence of calculated virial pressures on system (sorbate + sorbent) properties and composition can then be used to understand, interpret, and semi-quantitatively map/predict the nature and magnitude of forces that have the potential to induce pore collapse.

Isotherms from GEMC Simulations. These were carried out to yield water adsorption and desorption isotherms in NU-1000 at 298 K. During the adsorption half-cycle, the loadings range from ~12 molecules/unit cell at RH=25% to ~15 molecules/unit cell at RH=70% (**Figure S29**), with the former corresponding to water binding on the 12 H_2O/OH pairs present on the three Zr_6 nodes, and the latter corresponding to the adsorption of an additional 3 water molecules, each of which forms transient hydrogen-bonding bridges in the c-pore. The steep water uptake at RH~72% corresponds to mesopore filling. For the desorption branch, water evacuation occurs sequentially from the micropores (~70% and ~55% RH), to the mesopores (~47% RH), and to the *c*-pores (0% RH). The computational observation that water evacuation starts from micropores is consistent with these being the most hydrophobic feature of the pore environment. Further, the sequence of pore evacuation is in line with the MD simulations (below), as well as with experimental observations. The loading of ~550 water molecules per unit cell at saturation, ~1.5 g/g,[39] corresponds to ~400 waters in mesopores + *c*-pores, with the remaining ~150 waters filling the triangular micropores. When considering the pore-accessible volume, this loading is near the bulk liquid density of water (see **Figure S30**).

Molecular Dynamics Simulations. MD simulations for various water loadings in NU-1000 and its three variants were performed in the canonical ensemble (fixed loading and random initial positions of water molecules) to probe the water-induced stresses experienced during the evacuation process. The qualitative characteristics of the virial pressure, P_{wat}, as a function of the water loading (given here as ρ_{wat}) are the same for the three node chemistries considered here (**Figure 5a**). Off-diagonal components of the pressure tensor were examined and conveyed no additional information. When ρ_{wat} is decreased from its saturation loading (*i.e.*, 1.5 g water/g MOF), P_{wat} decreases sharply as water is homogeneously stretched within the porous matrix. A negative pressure of the water molecules indicates that contraction of the system would lower its potential energy, and such negative pressures can be observed experimentally in bulk water.[40] For the smallest system size studied here, 1×1×2 unit cells, two local minima for P_{wat} are observed for ρ_{wat}≈1.25 and ≈1.40 g/g that correspond to the reduction in the stress as water evacuates the triangular micropores that are less hydrophilic due to a paucity of node-based sites for H-bonding (**Figure 5b-ii-ix**). Maps of the number of hydrogen bonds that water molecules participate in as a function of location confirm that triangular channels are geometrically constraining, with waters near the walls involved in fewer hydrogen bonds (**Figures S31 & S32**). A broader minimum, P_{wat}^{cav}, follows near ρ_{wat}≈1.05 g/g just before cavitation of a bubble in the liquid occupying the mesopore

https://doi.org/10.26434/chemrxiv-2023-rvvfr **ORCID:** https://orcid.org/0000-0002-5024-1879 Content not peer-reviewed by ChemRxiv. **License:** CC BY-NC-ND 4.0

(**Figure 5b-x**). This finding supports our previous inference that the cavitation process in the mesopore contributes to the structural collapse during the 1st water desorption step. The inference is also supported by our simulated adsorption-desorption cycling over limited pressure regions that do not show hysteresis since filling-evacuation of the mesopore is not encountered (**Figure 3c,d**). The simulation data indicate that $|P_{wat}^{cav}|$ is largest for NU-1000, which is indeed most susceptible to collapse. Modification of nodes with chloride or formate ions reduces the stress during cavitation, following a pattern that corresponds to the ability of the ligands to participate in hydrogen bonds (if, for simplicity, we overlook the μ_3-hydroxo and μ_3-hydroxo ligands common to all versions, NU-1000 can donate or accept H-bonds, NU-1000-Cl can only accept, and NU-1000-formate cannot do either). It should be noted that the virial pressures reported are measures of the stress induced on the MOF and are distinct from the MOF's ability to withstand such stresses. Analysis of the simulation trajectories indicates nanobubbles are initially formed from density fluctuations along the hydrophobic walls of triangular pores and then expand to hexagonal pores (**Figure 5b**). The nanobubbles observed in the mesopore are rod-shaped and, as they grow, quickly extend through the entire periodic simulation box along the c-direction (*i.e.*, two unit-cells). The bubble tends to adhere to the walls of NU-1000 rather than forming in the center of the mesopore, as is observed for other guests, such as ammonia[41] and methanol (**Figure S33**). The locations of these bubbles within NU-1000 persist throughout the length of a simulation (**Figure S34**), despite that individual water molecules are able to explore the entire pore environment as indicated by molecular diffusion estimates from directional mean-square displacements (**Figure S35**).

As ρ_{wat} is decreased further, the volume of the bubbles increases and the pressure curve changes sign in its first and second derivatives and asymptotically approaches zero pressure from below, similar to the case of bulk liquid water.[15] This is true for all node chemistries considered (**Figure S36**). Analysis of simulation trajectories reveals that at exceptionally low densities (ρ_{wat}<0.15 g/g), the most favorable location for water is within the *c*-pore between two Zr_6 nodes, forming hydrogen bonded bridges between proximal nodes (**Figures S37**). Beyond the maximum loading of the *c*-pore itself, additional waters may localize within the micropores, so as to maintain hydrogen bonding with those confined in the *c*-pores. Beyond ρ_{wat}≈0.3 g/g, the hexagonal mesopore becomes preferable to triangular micropore (**Figure S37**). These sittings are consistent with a prior simulation study using a different force field.[42]

When the simulated system comprises only one unit cell in the *ab*-plane (two micropores and one mesopore), we find that complete evacuation of one micropore (*i.e.*, 50% of the micropores) is preferable to partial occupation of all micropores. For a more extended system in the *ab*-plane, we find a smoothing of the sawtooth pattern as emptying of one micropore corresponds to only a small fraction of the micropores (**Figure 5a**). Two local minima in P_{wat} persist, one at ρ_{wat}≈1.4 g/g corresponding to cavitation in the first micropore (above which the pore volume is filled with a homogeneously stretched liquid with no bubbles), and the other near ρ_{wat} ≈1.0 g/g, P_{wat}^{cav} (below which bubbles can be observed in the mesopores). Similar behavior in P_{wat} is observed when the unit cell is further replicated along the *c*-axis, although in this case the sawtooth pattern is smoothed out because the micropores are large/long enough to be partially filled after bubble nucleation (**Figure S38**). Across all system sizes investigated, $|P_{wat}|$ is greatest at P_{wat}^{cav}, preceding bubble nucleation in the mesopore, at a value of ρ_{wat} (ρ_{wat}^{cav}) at which all micropores are vacant. At densities lower than ρ_{wat}^{cav}, the combination of pores that are vacant is far less prescriptive, and micropores that were vacant at higher densities may re-fill (**Figure S39**). This unexpected behavior minimizes the surface area of the bubble, which may span multiple unit-cells laterally. At ρ_{wat} >ρ_{wat}^{cav}, a subset of micropores is vacant, and their distribution in the *ab*-plane is uncorrelated (**Figure 5b(i)-(ix)**).

CONCLUSIONS

Crucial for many applications of MOFs is mitigation of structural damage caused by capillary forces associated with evacuation of water from MOF pores. We find that the nature and magnitude of these forces can be quantitatively understood by framing evacuation in terms of nanocavitation. When coupled with molecular dynamics data, nanocavitation-centered modeling discloses the dependence of forces on pore loading, pore size, pore identity, and pore composition, and reveals why sorbed water presents unique challenges. Experimental isotherms, DED, and XAS measurements with five variants of NU-1000 validate and corroborate the computational findings, including findings regarding sequence of pore-filling, mitigation of capillary forces, and MOF compositional stabilization against water-evacuation-based structural degradation.

ASSOCIATED CONTENT

Supporting Information. Experimental procedures, X-ray absorption (XAS) spectra, powder X-ray diffraction (PXRD) patterns, N_2 and water isotherms, pore size distribution, difference envelope density (DED) plots, NMR spectra, and simulation details are available free of charge *via* the Internet at http://pubs.acs.org.

AUTHOR INFORMATION

Corresponding Authors

* Jian Liu: kjlsch@rit.edu;
* J. Ilja Siepmann: siepmann@umn.edu;
* Joseph T. Hupp: j-hupp@northwestern.edu.

ACKNOWLEDGMENT

This work was primarily supported by the Department of Energy, Office of Basic Energy Sciences, Division of Chemical Sciences, Geosciences and Biosciences under Awards DE-FG02-08ER15967 (synthesis and measurements) and DE-FG02-17ER16362/DE-SC0023454 (molecular modeling). This work used IMSERC X-RAY facility at NU, which received support from SHyNE Resource (NSF ECCS-2025633), and Northwestern University. The REACT Facility of the NU REACT Center is supported by DOE (DE-SC0001329). Part of the computer resources was provided by the Minnesota Supercomputing Institute. Boris V. Kramar is partially supported by a MURI Grant from ONR (N00014-20-1-2517). The effort of Lin X. Chen is partially supported by the U.S. Department of Energy, Office of Science, Office of Basic Energy Sciences, under Contract No. DE-AC02-06CH11357.

https://doi.org/10.26434/chemrxiv-2023-rvvfr **ORCID:** https://orcid.org/0000-0002-5024-1879 Content not peer-reviewed by ChemRxiv. **License:** CC BY-NC-ND 4.0

REFERENCES

(1) Shi, Y.; Xie, Y.; Alshahrani, T.; Chen, B. A Zirconium-based Microporous Metal–Organic Frameworks for Molecular Sieving CO_2 Separation. *CrystEngComm.* **2023**, *25*, 1643-1647.

(2) Barnett, B. R.; Parker, S. T.; Paley, M. V.; Gonzalez, M. I.; Biggins, N.; Oktawiec, J.; Long, J. R. Thermodynamic Separation of 1-Butene from 2-Butene in Metal–Organic Frameworks with Open Metal Sites. *J. Am. Chem. Soc.* **2019**, *141*, 18325-18333.

(3) Wang, X.; Lan, P. C.; Ma, S. Metal-Organic Frameworks for Enzyme Immobilization: Beyond Host Matrix Materials. *ACS Cent. Sci.* **2020**, *6*, 1497-1506.

(4) Dhaka, S.; Kumar, R.; Deep, A.; Kurade, M. B.; Ji, S.-W.; Jeon, B.-H. Metal–Organic Frameworks (MOFs) for the Removal of Emerging Contaminants from Aquatic Environments. *Coord. Chem. Rev.* **2019,** *380*, 330-352.

(5) Liu, X.; Wang, X.; Kapteijn, F. Water and Metal-Organic Frameworks: From Interaction toward Utilization. *Chem. Rev.* **2020**, *120*, 8303-8377.

(6) Coudert, F. Water Adsorption in Soft and Heterogeneous Nanopores. *Acc. Chem. Res.* **2020**, *53*, 1342-1350.

(7) Park, K. S.; Ni, Z.; Cote, A. P.; Choi, J. Y.; Huang, R.; Uribe-Romo, F. J.; Chae, H. K.; O'Keeffe, M.; & Yaghi, O. M. Exceptional Chemical and Thermal Stability of Zeolitic Imidazolate Frameworks. *PNAS*, **2006**, *103*, 10186-10191.

(8) Abtab, S. M. T.; Alezi, D.; Bhatt, P. M.; Shkurenko, A.; Belmabkhout, Y.; Aggarwal, H.; Weselinski, L. J.; Alsadun, N.; Samin, U.; Hedhili, M. N.; Eddaoudi, M. Reticular Chemistry in Action: A Hydrolytically Stable MOF Capturing Twice Its Weight in Adsorbed Water. *Chem*, **2018**, *4*, 94-105.

(9) Low, J. J.; Benin, A. I.; Jakubczak, P.; Abrahamian, J. F.; Faheem, S. A.; & Wills R. R. Virtual High throughput Screening Confirmed Experimentally: Porous Coordination Polymer Hydration. *J. Am. Chem. Soc.* **2009**, *131*, 15834-15842.

(10) Furukawa, H.; Gandara, F.; Zhang, Y.; Jiang, J.; Queen, W. L.; Hudson, M. R.; & Yaghi, O. M. Water Adsorption in Porous Metal–Organic Frameworks and Related Materials. *J. Am. Chem. Soc.* **2014**, *136*, 4369-4381.

(11) Hanikel, N.; Prevot, M. S.; & Yaghi, O. M. MOF Water Harvesters. *Nat. Nanotechnol.* **2020**, *15*, 348-355.

(12) Rieth, A. J.; Wright, A. M.; Rao, S.; Kim, H.; LaPotin A. D.; Wang, E. N.; & Dinca M. Tunable Metal–Organic Frameworks Enable High-Efficiency Cascaded Adsorption Heat Pumps. *J. Am. Chem. Soc.* **2018**, *140*, 17591-17596.

(13) Islamoglu, T.; Chen, Z.; Wasson, M. C.; Buru, C. T.; Kirlikovali, K. O.; Afrin, U.; Mian, M. R.; & Farha, O. K. Metal–Organic Frameworks against Toxic Chemicals. *Chem. Rev.* **2020**, *120*, 8130-8160.

(14) Kirlikovali, K. O.; Chen, Z.; Islamoglu, T.; Hupp, J. T.; Farha, O. K. Zirconium-Based Metal-Organic Framework for the Catalysis of Organophosphorus Nerve Agents. *ACS Appl. Mater. Interfaces*, **2020**, *12*, 14702-14720.

(15) Chen, J. L.; Xue, B.; Mahesh, K.; & Siepmann, J. I. Molecular Simulations Probing the Thermophysical Properties of Homogeneously Stretched and Bubbly Water Systems. *J. Chem. Eng. Data* **2019**, *64*, 3755-3771.

(16) Lu, Z.; Liu, J.; Zhang, X.; Liao, Y.; Wang, R.; Zhang, K.; Lyu, J.; Farha, O. K.; & Hupp J. T. Node-Accessible Zirconium MOFs. *J. Am. Chem. Soc.* **2020**, *142*, 21110-21121.

(17) Liu, J.; Lu, Z.; Chen, Z.; Rimoldi, M.; Howarth, A. J.; Chen, H.; Alayoglu, S.; Snurr, R. Q.; Farha, O. K.; & Hupp, J. T. Ammonia Capture with Zirconium Metal–Organic Frameworks: Reversible and Irreversible Uptake. *ACS Appl. Mater. Interfaces* **2021**, *13*, 20081-20093.

(18) Liu, J.; Chen, Z.; Wang, R.; Alayoglu, S.; Islamoglu, T.; Lee, S.; Sheridan, T. R.; Chen, H.; Snurr, R. Q.; Farha, O. K.; & Hupp, J. T. Zirconium Metal–Organic Frameworks Integrating Chloride Ions for Ammonia Capture and/or Chemical Separation. *ACS Appl. Mater. Interfaces* **2021**, *13*, 22485-22494.

(19) Peters, A. W.; Otake, K.; Platero-Prats, A. E.; Li, Z.; DeStefano, M. R.; Chapman, K. W.; Farha, O. K.; & Hupp, J. T. Site-Directed Synthesis of Cobalt Oxide Clusters in a Metal–Organic Framework. *ACS Appl. Mater. Interfaces* **2018**, *10*, 15073-15078.

(20) Liu, J.; Li, Z.; Zhang, X.; Otake, K.; Zhang, L.; Peters, A. W.; Young, M. J.; Bedford, N. M.; Letourneau, S. P.; Mandia, D. J.; Elam, J. W.; Farha, O. K.; & Hupp J. T. Introducing Non-Structural Ligands to Zirconia-Like Metal–Organic Framework Nodes to Tune the Activity of Node-Supported Nickel Catalysts for Ethylene Hydrogenation. *ACS Catal.* **2019**, *9*, 3198–3207.

(21) Deria, P.; Chung, Y. G.; Snurr, R. Q.; Hupp, J. T.; & Farha, O. K. *Chem. Sci.* **2015**, *6*, 5172-5176.

(22) Liu, J.; Anderson, R.; Schmalbach, K. M.; Sheridan, T. R.; Wang, Z.; Schweitzer, N. M.; Stein, A.; Mara, N. A.; Gomez-Gualdron, D.; & Hupp, J. T. Insights into Dual-Functional Modification for Water Stability Enhancement of Mesoporous Zirconium Metal–Organic Frameworks. *J. Mater. Chem. A* **2022**, *10*, 17307-17316.

(23) Yang, D.; Ortuno, M. A.; Bernales, V.; Cramer, C. J.; Gagliardi, L.; Gates, B. C. Structure and Dynamics of Zr_6O_8 Metal–Organic Framework Node Surfaces Probed with Ethanol Dehydration as a Catalytic Test Reaction. *J. Am. Chem. Soc.* **2018**, *140*, 3751-3759.

(24) Islamoglu, T.; Otake, K.-i.; Li, P.; Buru, C. T.; Peters, A. W.; Akpinar, I.; Garibay, S. J.; Farha, O. K. Revisiting the Structural Homogeneity of NU-1000, a Zr-based Metal–Organic Framework. *CrystEngComm* **2018**, *20*, 5913-5918.

(25) Webber, T. E.; Liu, W.; Desai, S. P.; Lu, C. C.; Truhlar, D. G.; Penn, R. L. Role of a Modulator in the Synthesis of Phase-Pure NU-1000. *ACS Appl. Mater. Interfaces*, **2017**, *9*, 39342-39346.

(26) Drache, F.; Cirujano, F. G.; Nguyen, K. D.; Bon, V.; Senkovska, I.; Llabrés i Xamena, F. X.; Kaskel, S. Anion Exchange and Catalytic Functionalization of the Zirconium-Based Metal–Organic Framework DUT-67. *Cryst. Growth Des.* **2018**, *18*, 5492-5500.

(27) Rieth, A. J.; Wright, A. M.; Skorupskii, G.; Mancuso, J. L.; Hendon, C. H.; Dinca, M. Record-Setting Sorbents for Reversible Water Uptake by Systematic Anion Exchanges in Metal–Organic Frameworks. *J. Am. Chem. Soc.* **2019**, *141*, 13858-13866.

(28) Akiyama, G.; Matsuda, R.; Kitagawa, S. Highly Porous and Stable Coordination Polymers as Water Sorption Materials. *Chem. Lett.* **2010**, *39*, 360-361.

(29) Lu, Z.; Duan, J.; Du, L.; Liu, Q.; Schweitzer, N. M.; Hupp, J. T. Incorporation of Free Halide Ions Stabilizes Metal–Organic Frameworks (MOFs) against Pore Collapse and Renders Large-Pore Zr-MOFs Functional for Water Harvesting. *J. Mater. Chem. A* **2022**, *10*, 6442-6447.

(30) DeCoste, J. B.; Peterson, G. W.; Jasuja, H.; Glover, T. G.; Huang, Y.-g.; Walton, K. S. Stability and Degradation Mechanisms of Metal–Organic Frameworks Containing the $Zr_6O_4(OH)_4$ Secondary Building Unit. *J. Mater. Chem. A* **2013**, *1*, 5642-5650.

(31) Platero-Prats, A. E.; Mavrandonakis A.; Liu, J.; Chen, Z.; Chen, Z.; Li, Z.; Yakovenko, A. A.; Gallington, L. C.; Hupp, J. T.; Farha, O. K.; Cramer, C. J.; Chapman, K. W. The Molecular Path Approaching the Active Site in Catalytic Metal–Organic Frameworks. *J. Am. Chem. Soc.* **2021**, *143*, 20090-20094.

(32) Burtch, N. C.; Walton, I. M.; Hungerford, J. T.; Morelock, C. R.; Jiao, Y.; Heinen, J.; Chen, Y.; Yakovenko, A. A.; Xu, W.; Dubbeldam, D.; Walton, K. S. In Situ Visualization of Loading-Dependent Water Effects in a Stable Metal–Organic Framework. *Nat. Chem.* **2020**, *12*, 186-192.

(33) Yang, Y.; Noh, H.; Ma, Q.; Wang, R.; Chen, Z.; Schweitzer, N. M.; Liu, J.; Chapman, K. W.; Hupp, J. T. Engineering Dendrimer-Templated, Metal–Organic Framework-Confined Zero-Valent, Transition-Metal Catalysts. *ACS Appl. Mater. Interfaces* **2021**, *13*, 36232-36239.

(34) Yakovenko, A. A.; Wei, Z.; Wriedt, M., Li, J.; Halder, G. J.; Zhou, H. Study of Guest Molecules in Metal-Organic Frameworks by Powder X-ray Diffraction: Analysis of Difference Envelope Density. *Cryst. Growth Des.* **2014**, *14*, 5397-5407.

(35) Lucier, B. E. G.; Chen, S.; Huang, Y. Characterization of Metal-Organic Frameworks: Unlocking the Potential of Solid-State NMR. *Acc. Chem. Res.* **2018**, *51*, 319-330.

https://doi.org/10.26434/chemrxiv-2023-rvvfr **ORCID:** https://orcid.org/0000-0002-5024-1879 Content not peer-reviewed by ChemRxiv. **License:** CC BY-NC-ND 4.0

(36) Koschnick, C.; Staglich, R.; Scholz, T.; Terban, M. W.; von Mankowski, A.; Savasci, G.; Binder, F.; Schokel, A.; Etter, M.; Nuss, J.; Siegel, R.; Germann, L. S.; Ochsenfeld, C.; Dinnebier, R. E.; Senker, J.; Lotsch, B. V. Understanding Disorder and Linker Deficiency in Porphyrinic Zirconium-Based Metal-Organic Frameworks by Resolving the Zr_8O_6 Cluster Conundrum in PCN-221. *Nat. Commun.* **2021**, *12*, 3099.
(37) Ogiwara, N.; Kobayashi, H.; Inukai, M.; Nishiyama, Y.; Concepcion, P.; Rey, F.; Kitagawa, H. Ligand-Functionalization-Controlled Activity of Metal-Organic Framework-Encapsulated Pt Nanocatalyst toward Activation of Water. *Nano Lett.* **2020**, *20*, 426-432.
(38) Wang, R.; Shi, K.; Liu, J.; Snurr, R. Q.; Hupp, J. T. Water-Accelerated Transport: Vapor-Phase Nerve Agent Simulant Delivery within a Catalytic Zirconium Metal-Organic Framework as a Function of Relative Humidity. *J. Am. Chem. Soc.*, **2023**, DOI: 10.1021/jacs.3c03708.
(39) The different water loading in NU-1000 at saturation between experimental (1.14g/g) and theoretical (1.50g/g) studies presumably results from the contraction of MOF pores due to thermal treatment prior to the water isotherm measurements.
(40) Davitt, K.; Rolley, E.; Caupin, F.; Arvengas, A.; Balibar, S. Equation of State of Water under Negative Pressure. *J. Chem. Phys.* **2010**, *133*, 174507.
(41) Liu, Z.; An, G.; Xia, X.; Wu, S.; Li, S.; Wang, L. The Potential Use of Metal–Organic Framework/Ammonia Working Pairs in Adsorption Chillers. *J. Mater. Chem. A* **2021**, *9*, 6188-6195.
(42) Oliver, M. C.; Wang, S.; Huang, L.; Kasule, M.; & Wu, Y. Vapor-Like Water in the NU-1000 Zr-MOF: A Molecular Level Understanding of Balanced Hydrophobicity in Humid Conditions. *J. Phys. Chem. C*, **2023**, *127*, 6503-6514.

https://doi.org/10.26434/chemrxiv-2023-rvvfr **ORCID:** https://orcid.org/0000-0002-5024-1879 Content not peer-reviewed by ChemRxiv. **License:** CC BY-NC-ND 4.0

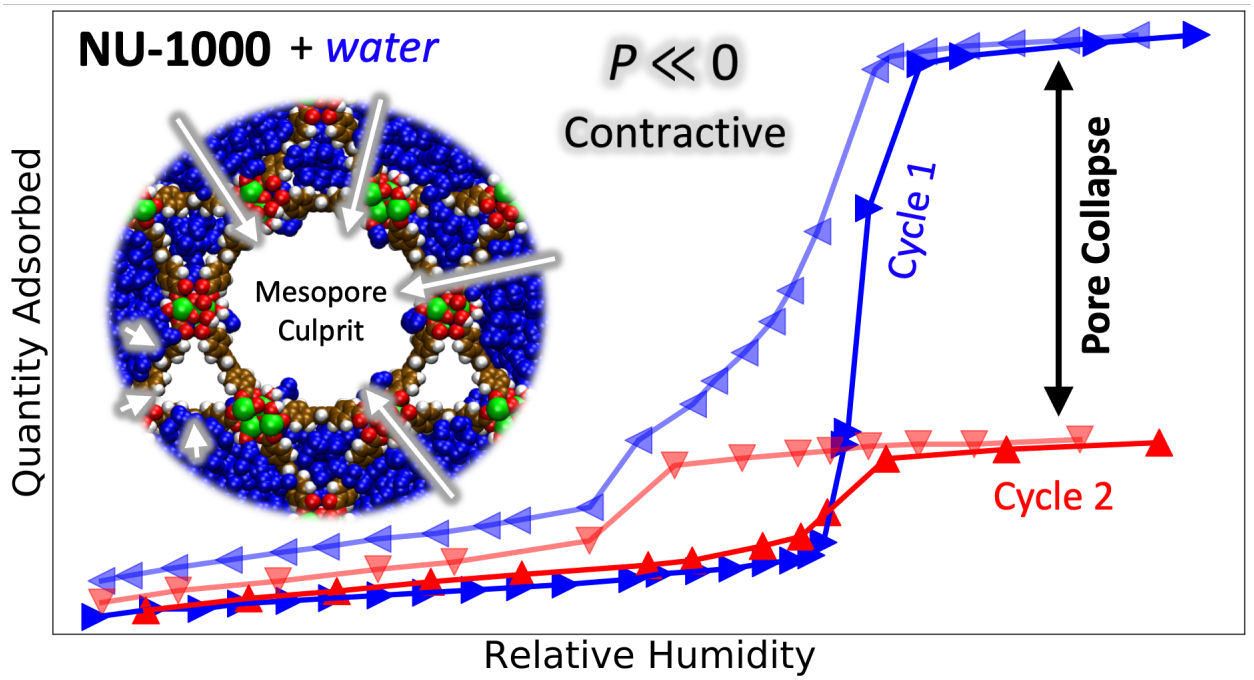

Insert Table of Contents artwork here

https://doi.org/10.26434/chemrxiv-2023-rvvfr **ORCID:** https://orcid.org/0000-0002-5024-1879 Content not peer-reviewed by ChemRxiv. **License:** CC BY-NC-ND 4.0